

# Nd isotope variation between the Earth–Moon system and enstatite chondrites

<https://doi.org/10.1038/s41586-022-05265-0>

Received: 4 February 2022

Accepted: 23 August 2022

Published online: 6 October 2022

 Check for updates

Shelby Johnston<sup>1</sup>, Alan Brandon<sup>1✉</sup>, Claire McLeod<sup>2</sup>, Kai Rankenburg<sup>3</sup>, Harry Becker<sup>4</sup> & Peter Copeland<sup>1</sup>

Reconstructing the building blocks that made Earth and the Moon is critical to constrain their formation and compositional evolution to the present. Neodymium (Nd) isotopes identify these building blocks by fingerprinting nucleosynthetic components. In addition, the  $^{146}\text{Sm}$ – $^{142}\text{Nd}$  and  $^{147}\text{Sm}$ – $^{143}\text{Nd}$  decay systems, with half-lives of 103 million years and 108 billion years, respectively, track potential differences in their samarium (Sm)/Nd ratios. The difference in Earth's present-day  $^{142}\text{Nd}/^{144}\text{Nd}$  ratio compared with chondrites<sup>1,2</sup>, and in particular enstatite chondrites, is interpreted as nucleosynthetic isotope variation in the protoplanetary disk. This necessitates that chondrite parent bodies have the same Sm/Nd ratio as Earth's precursor materials<sup>2</sup>. Here we show that Earth and the Moon instead had a Sm/Nd ratio approximately  $2.4 \pm 0.5$  per cent higher than the average for chondrites and that the initial  $^{142}\text{Nd}/^{144}\text{Nd}$  ratio of Earth's precursor materials is more similar to that of enstatite chondrites than previously proposed<sup>1,2</sup>. The difference in the Sm/Nd ratio between Earth and chondrites probably reflects the mineralogical distribution owing to mixing processes within the inner protoplanetary disk. This observation simplifies lunar differentiation to a single stage from formation to solidification of a lunar magma ocean<sup>3</sup>. This also indicates that no Sm/Nd fractionation occurred between the materials that made Earth and the Moon in the Moon-forming giant impact.

The isotopic variation among the meteorite groups, Earth and the Moon reflect an inhomogeneous distribution of pre-solar grains in the protoplanetary disk that carry large differences in isotopes such as  $^{48}\text{Ca}$ ,  $^{50}\text{Ti}$ ,  $^{54}\text{Cr}$ ,  $^{62}\text{Ni}$ ,  $^{94}\text{Mo}$  and  $^{95}\text{Mo}$ , and constrain their nucleosynthetic make-up<sup>4–6</sup>. For these isotope systems, Earth and the Moon are similar to enstatite chondrites but different from ordinary and carbonaceous chondrites. This is consistent with the precursor materials for Earth, the Moon and enstatite chondrites being primarily derived from the inner protoplanetary disk, and those for ordinary and carbonaceous chondrites being derived farther away from the protosun with varying amounts of s-process versus r-process isotopes<sup>4–6</sup>. For neodymium (Nd) isotopes, this comparison is more complex. This is because the present-day differences in  $^{142}\text{Nd}/^{144}\text{Nd}$  ratios between chondrites and Earth may reflect slow neutron-capture process (s-process) and/or rapid neutron-capture process (r-process) variation, different samarium (Sm)/Nd ratios with consequent differences in radiogenic  $^{142}\text{Nd}$  produced from  $^{146}\text{Sm}$  decay over Solar System history, or a combination of the two. Furthermore, the differences in their Sm/Nd ratios may reflect their precursor materials or may result from Earth's early differentiation. Differences in their Sm/Nd ratios was previously ruled out in favour of the differences in the  $^{142}\text{Nd}/^{144}\text{Nd}$  ratio in the present-day accessible Earth, which was approximately 10 ppm larger than for enstatite chondrites, being solely a result of s-process nucleosynthetic isotope differences<sup>1,2</sup>. In this scenario, Earth's precursor materials and enstatite chondrite parent bodies had the same Sm/Nd ratio. No difference of radiogenic

$^{142}\text{Nd}$  build-up occurred in Earth relative to these meteorite parent bodies from the onset of Solar System formation to the present. Here we show that the relationship between the Nd isotopic compositions of enstatite chondrites and Earth does not solely result from s-process differences. Instead, Earth had an Sm/Nd ratio approximately 2.4% higher than chondrites. To show this, we apply constraints for Nd isotope systematics obtained from the Moon. These findings help resolve the question of how compositional differences and similarities between enstatite chondrites, Earth and the Moon arose through early nebular mixing processes in the inner protoplanetary disk. These comparisons also aid in evaluating formation and early lunar differentiation models.

## Nd in chondrites, Earth and the Moon

We report high-precision Nd isotope measurements for 22 enstatite chondrites and 2 Allende CV3 chondrite fractions (Table 1, and Supplementary Tables 1 and 2). Sm and Nd were purified using column chromatography. Sm and Nd isotope measurements were made on thermal ionization mass spectrometers. The chondrite  $^{142}\text{Nd}/^{144}\text{Nd}$  ratios are corrected for radiogenic ingrowth differences of  $^{142}\text{Nd}$  using  $^{147}\text{Sm}/^{144}\text{Nd}$  ratios calculated from measured  $^{143}\text{Nd}/^{144}\text{Nd}$  ratios, then corrected to present-day values relative to the chondrite uniform reservoir (CHUR) for  $^{147}\text{Sm}/^{144}\text{Nd}$  and  $^{143}\text{Nd}/^{144}\text{Nd}$ <sup>1,2,7–9</sup> (Methods and Supplementary Table 3). The data for each isotope are presented in  $\mu$  notation, for example, where  $\mu^{142}\text{Nd}_{\text{corr}}$  is the parts in  $10^6$  (ppm) deviation for

<sup>1</sup>Department of Earth and Atmospheric Sciences, University of Houston, Houston, TX, USA. <sup>2</sup>Department of Geology and Environmental Earth Science, Miami University, Oxford, OH, USA.

<sup>3</sup>John De Laeter Centre, Curtin University, Bentley, Western Australia, Australia. <sup>4</sup>Freie Universität, Berlin, Germany. ✉e-mail: [abrandon@uh.edu](mailto:abrandon@uh.edu)

Table 1 | Nd isotope compositions of enstatite chondrites and Allende measured in this study

| Sample                  | Type  | $\mu^{142}\text{Nd}$ measured | $\mu^{142}\text{Nd}_{\text{corr}}$ | 2 s.e. | $\mu^{145}\text{Nd}$ | 2 s.e. | $\mu^{148}\text{Nd}$ | 2 s.e. | $\mu^{150}\text{Nd}$ | 2 s.e. | $^{147}\text{Sm}/^{144}\text{Nd}$ measured |
|-------------------------|-------|-------------------------------|------------------------------------|--------|----------------------|--------|----------------------|--------|----------------------|--------|--|
| Enstatite chondrites    |       |                               |                                    |        |                      |        |                      |        |                      |        |  |
| UH                      |       |                               |                                    |        |                      |        |                      |        |                      |        |  |
| LEW 87223               | EL3   | −2.7                          | 2.5                                | 7.8    | 2.0                  | 5.7    | −15.5                | 12.0   | 17.2                 | 25.0   | 0.1926                                     |
| MAC 02839               | EL3   | −8.6                          | −10.4                              | 12.2   | 2.1                  | 6.3    | 8.2                  | 17.0   | 47.7                 | 25.8   | 0.2053                                     |
| PCA 91020               | EL3   | −17.4                         | −18.4                              | 13.0   | 2.7                  | 11.8   | 6.1                  | 17.8   | 77.1                 | 26.9   |  |
| MAC 02747               | EL4   | −9.6                          | −9.6                               | 5.3    | 0.7                  | 3.2    | 5.8                  | 8.7    | 17.5                 | 17.3   | 0.1709                                     |
| ALHA 81021              | EL6   | −11.1                         | −9.2                               | 4.0    | −2.3                 | 3.2    | 36.8                 | 7.5    | 110.7                | 12.7   | 0.1872                                     |
| GRO 95626               | EL6   | −9.3                          | −9.4                               | 7.0    | 0.9                  | 5.5    | 22.4                 | 10.8   | 23.9                 | 19.5   | 0.1841                                     |
| GRO 95517 (1)           | EH3   | −7.8                          | −11.4                              | 3.6    | −0.8                 | 3.2    | 7.8                  | 7.0    | 783.9                | 32.5   |  |
| GRO 95517 (2)           | EH3   | −11.5                         | −10.7                              | 3.0    | 2.5                  | 2.2    | 5.0                  | 4.6    | 349.7                | 9.3    | 0.1850                                     |
| LAR 06252               | EH3   | −97                           | −8.5                               | 4.6    | −1.7                 | 3.4    | 13.3                 | 7.0    | 372.9                | 13.1   | 0.1939                                     |
| MET 01018               | EH3   | −12.4                         | −10.2                              | 3.6    | 3.1                  | 2.6    | 15.0                 | 5.4    | 34.4                 | 10.6   | 0.1922                                     |
| MIL 07028               | EH3   | −7.8                          | −3.9                               | 3.2    | −3.2                 | 2.5    | 0.5                  | 6.2    | 15.2                 | 11.0   | 0.2411                                     |
| PCA 91238               | EH3   | −0.7                          | −0.7                               | 9.7    | −3.7                 | 8.4    | 8.5                  | 12.0   | 32.1                 | 21.4   |  |
| EET 88746               | EH4   | −11.5                         | −10.3                              | 5.7    | −1.4                 | 5.1    | 2.8                  | 8.7    | 65.8                 | 16.9   |  |
| EET 96341               | EH4/5 | −12.6                         | −11.2                              | 4.6    | −3.1                 | 3.7    | 18.6                 | 7.5    | 38.0                 | 17.3   | 0.1932                                     |
| EET 96135               | EH4/5 | −4.3                          | −2.9                               | 5.1    | 2.8                  | 3.7    | −7.1                 | 8.7    | 40.3                 | 17.8   | 0.2696                                     |
| EET 96299               | EH5/5 | −7.3                          | −6.0                               | 5.2    | 2.1                  | 3.6    | 1.2                  | 9.5    | 6.1                  | 15.9   | 0.1866                                     |
| LEW 88180               | EH5   | −7.8                          | −6.3                               | 4.9    | 0.9                  | 3.4    | 7.5                  | 7.9    | 35.6                 | 15.2   | 0.1912                                     |
| Berlin                  |       |                               |                                    |        |                      |        |                      |        |                      |        |  |
| MAC 88136 (1)           | EL3   | −5.6                          | −6.7                               | 3.2    | −0.1                 | 0.03   | 42.5                 | 5.2    | 9.2                  | 10.5   | 0.1953                                     |
| MAC 88136 (2)           | EL3   | −9.0                          | −10.1                              | 2.8    | −0.1                 | 0.02   | 44.7                 | 4.6    | 14.0                 | 8.3    |  |
| MAC 02747               | EL4   | −6.8                          | −6.9                               | 2.8    | −0.5                 | 0.02   | 36.5                 | 3.7    | −3.6                 | 7.1    | 0.1948                                     |
| Blithfield (1)          | EL3   | −4.0                          | −77.0                              | 3.9    | 27.8                 | 0.03   | 21.7                 | 7.3    | −4.4                 | 12.3   | 0.3418                                     |
| Blithfield (2)          | EL3   | −4.2                          | −77.2                              | 2.8    | 27.8                 | 0.12   | 72.5                 | 5.1    | 63.5                 | 8.9    |  |
| Blithfield (3)          | EL3   | −1.9                          | −74.9                              | 2.5    | 27.8                 | 0.02   | 13.4                 | 3.8    | −9.8                 | 8.0    |  |
| LON 94100               | EL6   | −5.7                          | −8.9                               | 2.4    | 0.7                  | 0.02   | 15.9                 | 3.5    | 16.1                 | 7.9    | 0.1969                                     |
| ALH 81021               | EL6   | −5.1                          | −11.1                              | 2.5    | 1.8                  | 0.02   | 38.7                 | 3.9    | −28.7                | 7.9    | 0.1978                                     |
| PCA 91461               | EH3   | −8.1                          | −7.3                               | 3.6    | −0.8                 | 0.03   | 27.4                 | 5.7    | 13.8                 | 11.9   | 0.1947                                     |
| KLE 98300               | EH3   | −10.3                         | −6.7                               | 2.7    | −1.9                 | 0.03   | 27.2                 | 4.6    | 6.7                  | 11.9   | 0.1945                                     |
| ALH 84170               | EH3   | −11.2                         | −11.1                              | 6.1    | −0.5                 | 0.04   | 22.1                 | 8.2    | 9.0                  | 18.7   | 0.1914                                     |
| EET 96341               | EH4/5 | −6.3                          | −6.3                               | 2.7    | −0.5                 | 0.02   | 62.9                 | 4.6    | 21.0                 | 8.5    | 0.1945                                     |
| Carbonaceous chondrites |       |                               |                                    |        |                      |        |                      |        |                      |        |  |
| Allende                 | CV3   | −21.3                         | −20.1                              | 3.0    | 2.9                  | 2.0    | 18.3                 | 4.4    | −17.3                | 9.1    |  |
| Allende SI              | CV3   | −25.7                         | −18.8                              | 3.3    | 0.9                  | 2.6    | 24.9                 | 5.5    | 3.1                  | 9.9    |  |

$\mu^{142}\text{Nd} = [(^{142}\text{Nd}/^{144}\text{Nd})_{\text{sample}} / (^{142}\text{Nd}/^{144}\text{Nd})_{\text{JNdi}} - 1] \times 10^6$ . Duplicate samples (shown as (1), (2) and (3)) are separate digestions, processed through column chemistry at separate times and run on separate filaments. Uncertainties for each sample are given as  $\pm 2$  s.e. (s.e. = standard error = standard deviation/ $\sqrt{n}$ , where  $n$  is the number of cycles per sample measurement).

the corrected  $^{142}\text{Nd}/^{144}\text{Nd}$  ratio from the average value of the measured JNdi Nd standard. The present-day accessible Earth represented by the JNdi standard, is defined as having  $\mu^{142}\text{Nd}$ ,  $\mu^{145}\text{Nd}$ ,  $\mu^{148}\text{Nd}$  and  $\mu^{150}\text{Nd}$  values of zero<sup>1–3</sup>. Analysis of the uncertainty for each of these  $\mu\text{Nd}$  values of the present-day accessible Earth is provided in Methods and is based on group averages of the JNdi standard and terrestrial samples calculated for a 95% confidence interval (CI). All  $\mu^{142}\text{Nd}_{\text{corr}}$  values for the chondrites are present-day values except where noted below and corrected to the same  $^{147}\text{Sm}/^{144}\text{Nd}_{\text{CHUR}}$  ratio of 0.1960. Differences in the present-day  $\mu^{142}\text{Nd}_{\text{corr}}$  values between samples reflect differences in their nucleosynthetic isotope compositions and thus also equate to the initial  $\mu^{142}\text{Nd}$  at the beginning of Solar System history<sup>1,2,8,9</sup>. Additional details are in Methods.

Data from this study are combined with previous high-precision Nd isotope analyses from chondrites, calcium–aluminium-rich inclusions (CAIs) from Allende, and terrestrial values, represented by the JNdi Nd

standard (Supplementary Table 1). The Nd isotope compositions of Allende and other carbonaceous chondrites are strongly influenced by CAIs, which host almost half of the Nd in Allende and exert a strong s-excess control on Allende's composition<sup>1,2,9</sup>. To better interpret the source material of Allende without these inclusions ( $\text{Allende}_{\text{corr}}$ ), mass-balance calculations<sup>1</sup> subtract the average Allende CAI component ( $n = 12$ ) from Allende analyses ( $n = 12$ ). The Nd isotope weighted averages for enstatite, ordinary and carbonaceous chondrites, Allende, CAIs from Allende, and  $\text{Allende}_{\text{corr}}$  (corrected for CAI contribution) are calculated for a 95% CI following previous Nd isotope studies<sup>1,8,9</sup> (Supplementary Tables 1, 4 and 5, and Methods).

Chondrite group averages have Nd isotope patterns with deficits in  $\mu^{142}\text{Nd}_{\text{corr}}$  and excesses in  $\mu^{145}\text{Nd}$ ,  $\mu^{148}\text{Nd}$  and  $\mu^{150}\text{Nd}$  compared with the JNdi terrestrial standard with  $\mu\text{Nd}$  values of zero (Extended Data Figs. 1 and 2). Averaged CAIs have Nd isotope patterns with a deficit in  $\mu^{142}\text{Nd}_{\text{corr}}$  and large deficits in  $\mu^{145}\text{Nd}$ ,  $\mu^{148}\text{Nd}$  and  $\mu^{150}\text{Nd}$ . The

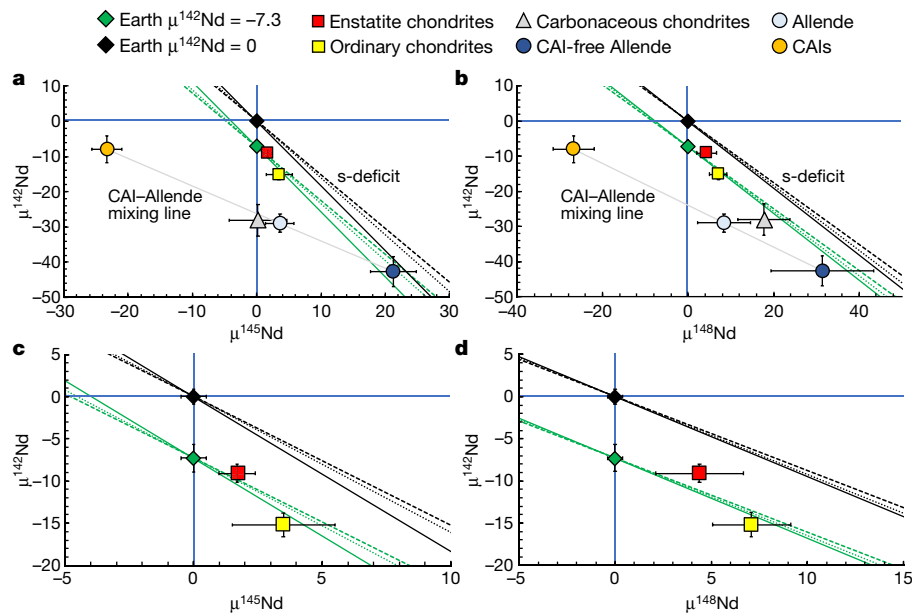


**Fig. 1 | Neodymium isotope variations of chondrites, CAIs and Earth.** Group averages are from Supplementary Tables 1 and 4 shown for enstatite chondrites ( $n=55$ ), ordinary chondrites ( $n=33$ ), carbonaceous chondrites ( $n=15$ ), CAIs ( $n=12$ ), Allende ( $n=12$ ) and Allende<sub>corr</sub> ( $n=12$ ). Error bars indicate the 95% CI for all group averages. The modelled s-deficit lines for an Earth with present-day  $\mu^{142}\text{Nd} = 0$  (black) and for an Earth with present-day  $\mu^{142}\text{Nd} = -7.3 \pm 1.6$  (green) are plotted. The s-deficit lines for the two Earth  $\mu^{142}\text{Nd}$  values are modelled for

stellar<sup>10</sup>, SiC pre-solar grains<sup>11</sup> and leachates<sup>12,34</sup> and are shown as solid, dotted and dashed lines, respectively. The mixing lines between CAIs and Allende<sub>corr</sub> that go through the Allende values are shown in solid grey. **a**,  $\mu^{142}\text{Nd}$  versus  $\mu^{145}\text{Nd}$ . **b**,  $\mu^{142}\text{Nd}$  versus  $\mu^{148}\text{Nd}$ . **c**, The same as **a** but zoomed into Earth, enstatite chondrites and ordinary chondrites. **d**, The same as **c** but for  $\mu^{142}\text{Nd}$  versus  $\mu^{148}\text{Nd}$ .

large deficits in  $\mu^{145}\text{Nd}$ ,  $\mu^{148}\text{Nd}$  and  $\mu^{150}\text{Nd}$  reflect excess of s-process isotopes relative to r-process Nd<sup>1</sup>. Enstatite chondrites have a mean  $\mu^{142}\text{Nd}_{\text{corr}} = -9.1 \pm 1.3$  (CI), ordinary chondrites have a mean  $\mu^{142}\text{Nd}_{\text{corr}} = -15.2 \pm 1.7$  (CI) and carbonaceous chondrites have a mean  $\mu^{142}\text{Nd}_{\text{corr}} = -28.1 \pm 5.9$  (CI) (Supplementary Table 4). The Allende<sub>corr</sub> group has a mean  $\mu^{142}\text{Nd}_{\text{corr}} = -42.7 \pm 5.2$  (CI). The  $\mu^{142}\text{Nd}_{\text{corr}}$ ,  $\mu^{145}\text{Nd}$  and  $\mu^{148}\text{Nd}$  relationships of these chondrite groups, CAIs, Allende<sub>corr</sub> and Earth are compared in Fig. 1. For the best-determined pairs with the lowest CI uncertainties on the group averages,  $\mu^{142}\text{Nd}_{\text{corr}}$  versus  $\mu^{145}\text{Nd}$  and  $\mu^{148}\text{Nd}$ , enstatite chondrite, ordinary chondrite and Allende<sub>corr</sub> group averages plot below s-deficit trends<sup>10–12</sup> passing through  $\mu^{142}\text{Nd} = 0.0 \pm 1.1$  (ref. <sup>1</sup>; Fig. 1). The group average values of  $\mu^{150}\text{Nd}$  are not as well determined with larger CI uncertainties (Methods). However, for  $\mu^{142}\text{Nd}_{\text{corr}}$  versus  $\mu^{150}\text{Nd}$ , averages plot below the s-deficit trends going through  $\mu^{142}\text{Nd} = 0.0 \pm 1.1$  as well (Extended Data Fig. 3). The exception is where the enstatite chondrite average overlaps on the lower side of the s-deficit trends going through  $\mu^{142}\text{Nd}$  and  $\mu^{150}\text{Nd} = 0 \pm 3.2$  (Extended Data Fig. 3c). All group averages use our data and all previous data from the literature and may reflect compositional or analytical bias for each average because each lab focused on a limited range of chondrite samples (Supplementary Table 1). One recent study measured 25 samples spanning the full compositional range of ordinary chondrites, enstatite chondrites and Allende<sup>1</sup>. The group averages reported in that study are within the CI uncertainties of the group averages calculated using all data from each lab for  $\mu^{142}\text{Nd}$ ,  $\mu^{145}\text{Nd}$ ,  $\mu^{148}\text{Nd}$  and  $\mu^{150}\text{Nd}$  (Extended Data Fig. 3). These also plot below s-deficit trends from  $\mu^{142}\text{Nd} = 0.0 \pm 1.1$ , including for  $\mu^{142}\text{Nd}$  versus  $\mu^{150}\text{Nd}$ . This confirms consistency between the different datasets from the different labs. For the  $\mu^{150}\text{Nd}$  values, this probably reflects analytical bias in the enstatite group average that is shifted to a higher value using data from all sources (Methods). The  $\mu^{150}\text{Nd}$  data from ref. <sup>1</sup> are interpreted as more representative.

These observations are inconsistent with a linear relationship between an Earth having  $\mu^{142}\text{Nd} = 0.0 \pm 1.1$ , versus  $\mu^{145}\text{Nd}$ ,  $\mu^{148}\text{Nd}$  and  $\mu^{150}\text{Nd}$ , and chondrites, via differences in the amounts of their s-process

components as previously proposed<sup>1</sup>. Another key result has been obtained in previous Nd isotopic work on lunar rocks. The present-day value for  $\mu^{142}\text{Nd}$ , calculated for precursor material for a single-stage differentiation of the Moon at  $4.39 \pm 0.015$  billion years ago (Ga) is  $-7.3 \pm 1.6$  ( $\pm 2\sigma$ )<sup>3,13</sup>. The  $\mu^{142}\text{Nd}$  value of  $-7.3 \pm 1.6$  is obtained from a York-fit regression of lunar basalts that provides this closure age for the Sm–Nd isotope system during lunar solidification<sup>3,13</sup>. The s-deficit lines align with a  $\mu^{142}\text{Nd} = -7.3 \pm 1.6$  trend through the enstatite, ordinary and Allende<sub>corr</sub> group averages (Fig. 1 and Extended Data Fig. 3). If Earth and the Moon formed from the same well mixed material in the Moon-forming giant impact, as is supported by multiple isotope proxies (for example, O, Ti and Cr<sup>14–16</sup>) then Earth probably had the same or nearly so initial  $\mu^{142}\text{Nd}$ . Thus, there may be a coincidence between the inferred  $\mu^{142}\text{Nd}$  of the bulk Moon and that for the bulk Earth. This means that the initial bulk Earth was lower in  $\mu^{142}\text{Nd}$  than proposed from terrestrial samples representing the present-day accessible Earth with a  $\mu^{142}\text{Nd} = 0.0 \pm 1.1$  (ref. <sup>17</sup>).

## Implications for Earth's Nd isotope composition

A bulk Earth derived from precursor materials with  $\mu^{142}\text{Nd} = -7.3 \pm 1.6$  resolves important questions about the Earth–Moon system and enstatite chondrites. First, it reduces the difference of the  $\mu^{142}\text{Nd}$  s-process nucleosynthetic anomaly between Earth and enstatite chondrites from a difference of approximately 10 ppm to 2 ppm. This is consistent with small but resolvable anomalies in  $\mu^{145}\text{Nd}$ ,  $\mu^{148}\text{Nd}$  and  $\mu^{150}\text{Nd}$ , and other isotopes such as <sup>50</sup>Ti, <sup>54</sup>Cr, <sup>62</sup>Ni, <sup>94</sup>Mo and <sup>95</sup>Mo (refs. <sup>1,5,6</sup>). Second, the Moon-forming giant impact must have been energetically intense enough to fully homogenize the materials that made both Earth and the Moon<sup>16,18</sup>, and/or the Mars-sized impactor was virtually identical to proto-Earth in isotopic composition for refractory elements<sup>19</sup>. This observation from Nd is thus an important constraint for Moon-forming giant impact models. Third, it simplifies the Moon's early differentiation history. Models previously favoured using  $\mu^{142}\text{Nd} = 0.0 \pm 1.1$  or a

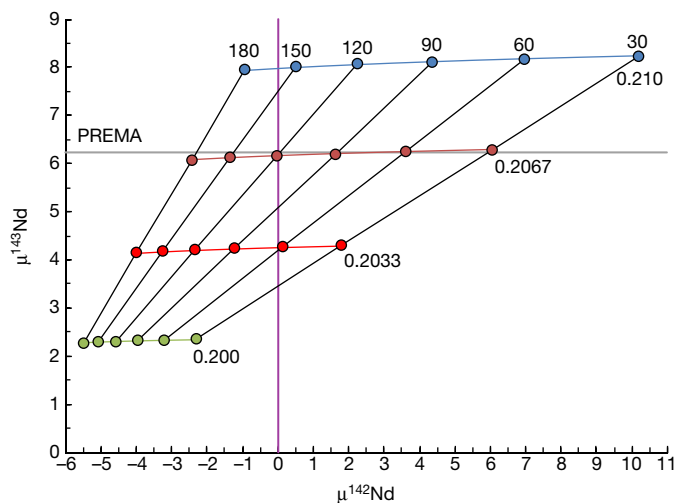


**Fig. 2 |  $\mu^{142}\text{Nd}$  versus  $\epsilon^{143}\text{Nd}$  for a single-stage collisional erosion model coincident with the Moon-forming giant impact.** The time in millions of years since Solar System formation at 4.568 Ga is shown for  $^{147}\text{Sm}/^{144}\text{Nd}$  fractionation from an initial chondritic value of 0.1960,  $\mu^{142}\text{Nd} = -7.3 \pm 1.6$  and  $\epsilon^{143}\text{Nd} = 0$ . The lines show resultant present-day values of  $\mu^{142}\text{Nd}$  and  $\epsilon^{143}\text{Nd}$  for  $^{147}\text{Sm}/^{144}\text{Nd}$  of 0.2000 (green), 0.2033 (red), 0.2067 (brown) and 0.2100 (blue) with 30 Myr increments shown as black lines for the Sm/Nd fractionation time from 30 Myr to 180 Myr after Solar System formation. The present-day PREMA value of  $\epsilon^{143}\text{Nd} = 6.2 \pm 0.7$  (ref.<sup>28</sup>) is shown as a grey band and the present-day Earth with  $\mu^{142}\text{Nd} = 0.0 \pm 1.1$  for the present-day accessible Earth (Methods) is shown as a purple band. The parameters and equations used are listed in Supplementary Table 6.

value similar to chondrites and more negative than  $-7.3 \pm 1.6$  (ref.<sup>3</sup>). These require multi-stage lunar differentiation histories before what is interpreted as final solidification/closure of the lunar magma ocean at  $4.39 \pm 0.015$  Ga (refs.<sup>3,13</sup>). The chronology and physical mechanisms for a multi-stage early lunar differentiation are not constrained<sup>3</sup>. Hence, a single-stage differentiation and cooling history, from lunar formation to solidification of a global magma ocean at  $4.39 \pm 0.015$  Ga, is more straightforward, and only the timing of the Moon-forming giant impact itself needs to be better known<sup>20</sup>.

Finally, this interpretation means that the present-day accessible Earth with a  $\mu^{142}\text{Nd} = 0.0 \pm 1.1$ , has an excess in the  $^{142}\text{Nd}/^{144}\text{Nd}$  ratio of about 7 ppm relative to its precursor materials with an initial  $\mu^{142}\text{Nd} = -7.3 \pm 1.6$ . These data lead us to consider four possible scenarios in the next section.

### Origin of excess $^{142}\text{Nd}$ in Earth

First, proton-capture nucleosynthesis (p-process) can form  $^{142}\text{Nd}$  (Extended Data Fig. 2). The excess in Earth relative to chondrites may represent additional p-process  $^{142}\text{Nd}$ . The correlations between  $\mu^{142}\text{Nd}$  and  $\mu^{145}\text{Nd}$ ,  $\mu^{148}\text{Nd}$  and  $\mu^{150}\text{Nd}$  along s-deficit lines between chondrites and an Earth–Moon system with  $\mu^{142}\text{Nd} = -7.3 \pm 1.6$  eliminates this scenario and indicates that the excess should be radiogenic  $^{142}\text{Nd}$  produced after Earth accreted.

Three other scenarios require radiogenic ingrowth of  $^{142}\text{Nd}$  with a larger Sm/Nd ratio than chondrites. In the second scenario, an enriched  $^{142}\text{Nd}$  silicate reservoir with a subchondritic Sm/Nd ratio was established in early Earth<sup>21</sup>. This reservoir, isolated near the core–mantle boundary, leaves a residual convecting mantle with a superchondritic Sm/Nd ratio evolving to the present-day with a more radiogenic  $^{142}\text{Nd}/^{144}\text{Nd}$  ratio for accessible Earth<sup>22</sup>. Evidence for these complementary reservoirs comes from Hadean samples having positive and negative  $\mu^{142}\text{Nd}$  of up to  $\pm 20$  (refs.<sup>23,24</sup>). The  $\mu^{142}\text{Nd}$  anomalies decrease over time to

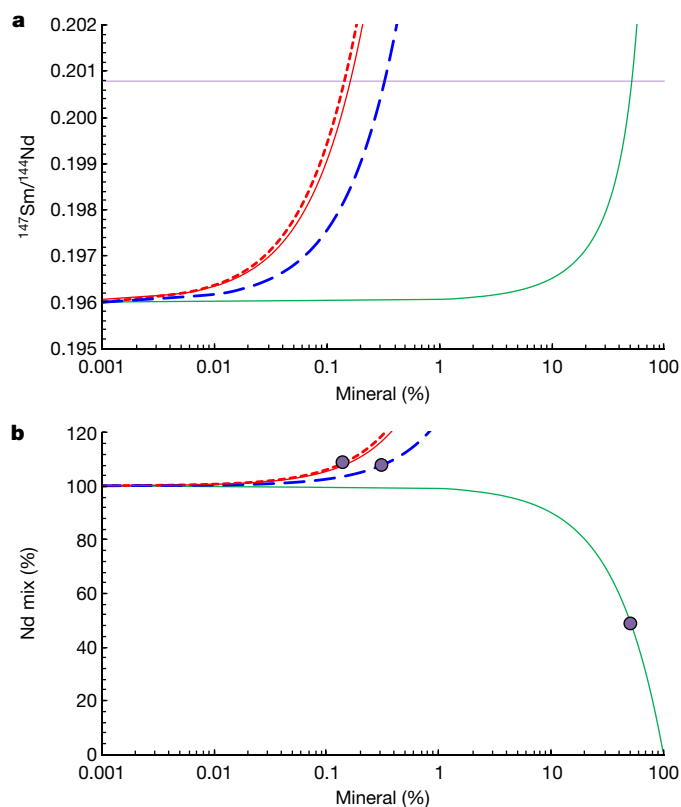


**Fig. 3 | Mixing models for enstatite chondrites with oldhamite and olivine.** The models use bulk CHUR  $^{147}\text{Sm}/^{144}\text{Nd}$  with average EH chondrite Sm and Nd abundances. The values used are listed in Supplementary Table 7. **a**, The  $^{147}\text{Sm}/^{144}\text{Nd}$  values versus percentage mineral in a mixture with bulk enstatite chondrite. The horizontal purple line is the target value of  $^{147}\text{Sm}/^{144}\text{Nd} = 0.20079$ . The red dashed line is a mix between enstatite chondrite and ALH77295 oldhamite; the red solid line is the same but with 10% forsterite added into the mix; the dashed blue line is for enstatite chondrite and ALH97072 oldhamite; the solid green line is for enstatite chondrite and forsterite. **b**, The percentage Nd abundance increase or decrease relative to bulk enstatite chondrite versus percentage of oldhamite and/or olivine added to the mix. The lines are same as in **a**. The purple circles are the percentage mineral for the models that hit the target value of  $^{147}\text{Sm}/^{144}\text{Nd} = 0.20079 \pm 0.00058$  for the precursor materials for the Earth–Moon system.

$\mu^{142}\text{Nd} = 0.0 \pm 1.1$  for late-Tertiary basalts<sup>17,24</sup>. Although remnants of an early-formed enriched silicate reservoir may still exist<sup>25</sup>, these relationships indicate that efficient convective stirring over 4 Gyr has established a present-day bulk at  $\mu^{142}\text{Nd} = 0.0 \pm 1.1$  (ref.<sup>24</sup>) such that this early enriched reservoir probably does not significantly contribute to the mass balance of Nd in the bulk Earth.

In a third scenario, the composition of early Earth is modified by the loss of silicate and, preferentially, incompatible-element-enriched proto-crust with a subchondritic Sm/Nd ratio through collisional erosion<sup>26</sup>. This possibly occurred during the Moon-forming giant impact<sup>26,27</sup>. Matching the bulk Earth superchondritic Fe/Mg ratio of  $2.1 \pm 0.1$ , that is, about 10% above the solar ratio of  $1.9 \pm 0.1$ , takes approximately 10% of silicate removal from collisional erosion<sup>26</sup>. The loss of this material leaves Earth depleted in incompatible trace elements and a superchondritic  $^{147}\text{Sm}/^{144}\text{Nd}$  ratio of up to 0.21 (ref.<sup>26</sup>). Here a present-day Earth with  $\mu^{142}\text{Nd} = 0.0 \pm 1.1$  from an initial  $\mu^{142}\text{Nd} = -7.3 \pm 1.6$  is evaluated for a single-stage collisional erosion event. The extent and timing of Sm/Nd fractionation is obtained from the consequent present-day  $\epsilon^{143}\text{Nd}$  (10<sup>4</sup> parts deviation from the average chondrite  $^{143}\text{Nd}/^{144}\text{Nd}$  ratio (CHUR)<sup>7</sup>) (Fig. 2). Reaching  $^{147}\text{Sm}/^{144}\text{Nd} = 0.21$  ( $f_{\text{Sm/Nd}} = 1.07$ , or 7% fractional difference ( $f$ ) from  $^{147}\text{Sm}/^{144}\text{Nd}_{\text{CHUR}} = 0.1960$ ) with

a match of  $\epsilon^{143}\text{Nd} = +8$  and  $\mu^{142}\text{Nd} = 0.0 \pm 1.1$  for mid-ocean ridge basalts, which are thought to represent the composition of the material making the present-day bulk convecting mantle<sup>26,28</sup>, is only possible with a Moon-forming giant impact as late as 180 Myr to 140 Myr after Solar System formation. A lower  $^{147}\text{Sm}/^{144}\text{Nd} = 0.20$  ( $f_{\text{Sm}/\text{Nd}} = 1.02$ ) does not result in enough  $^{142}\text{Nd}$  ingrowth such that  $\mu^{142}\text{Nd} = 0$  is reached at any time for the Moon-forming giant impact. The purported prevalent mantle (PREMA) composition with  $\epsilon^{143}\text{Nd} = +6.2 \pm 0.7$ , which may instead represent the early Earth bulk mantle composition<sup>28</sup>, is reached with  $f_{\text{Sm}/\text{Nd}} = 1.055$  and a Moon-forming giant impact 150 Myr to 100 Myr after Solar System formation. The PREMA or mid-ocean-ridge-basalt Nd isotope compositions require collisional erosion in a Moon-forming giant impact to be 4.468 Ga (100 Myr after Solar System formation) or later (Fig. 2). This is inconsistent with evidence supporting an earlier Moon-forming giant impact of  $>4.5$  Ga (ref. 20), although, as noted above, its timing is at present unclear. Another important challenge to a collisional erosion scenario is that consequent removal of incompatible trace elements and  $\geq 5\%$  change in the Sm/Nd ratio also means a reduction in the heat-producing elements U, Th and K, by as much as 50%, requiring unrealistic cooling rates of Earth through geologic time<sup>29</sup>.

In a fourth scenario, favoured here, the Earth–Moon system form from precursor materials in the inner protoplanetary disk with different Sm/Nd ratios and small differences of s-process isotopes relative to enstatite chondrites. Early thermochemical evolution and mixing in the protoplanetary disk may have resulted in precursor materials from adjacent Earth–Moon and enstatite chondrite precursors with distinct major-element compositions<sup>4,30,31</sup>. This probably resulted in the Earth–Moon precursors with a larger amount of olivine relative to enstatite chondrite precursors<sup>30</sup>. Preferential incorporation of olivine, enstatite and/or other refractory minerals in the precursor materials could lead to different Sm/Nd ratios between the Earth–Moon system and enstatite chondrites. An Earth–Moon system with an initial  $\mu^{142}\text{Nd} = -7.3 \pm 1.6$  reaches present-day  $\mu^{142}\text{Nd} = 0.0 \pm 1.1$  with a  $^{147}\text{Sm}/^{144}\text{Nd} = 0.20079 \pm 0.00058$  ( $2.4 \pm 0.5\%$  larger than the average chondrite value of 0.1960). This results in an  $\epsilon^{143}\text{Nd}$  of  $+2.8 \pm 0.3$ , intermediate between PREMA and CHUR. In enstatite chondrites, olivines have superchondritic Sm/Nd ratios with Sm and Nd abundances of a few parts per billion<sup>32</sup>. To obtain  $^{147}\text{Sm}/^{144}\text{Nd} = 0.20079 \pm 0.00058$  in Earth–Moon precursor materials, more than 50 wt% olivine must be added to enstatite chondrite material (Fig. 3a and Supplementary Table 7). This leaves resultant materials depleted in incompatible trace elements such as Nd by as much as 50% (Fig. 3b), and strongly reduced in heat-producing elements similar to collisional erosion. This indicates that olivine enrichment in the Earth–Moon precursor materials relative to enstatite chondrites was probably not a viable explanation for the elevated Sm/Nd.

An alternative is that the Earth–Moon precursor materials were enriched in oldhamite (CaS). Oldhamite is 0.1% to 1.6% by volume and comprises  $\geq 50\%$  of the rare-earth-element budget in enstatite chondrites<sup>33</sup>. Like olivine, oldhamite is a refractory mineral and condenses early in the strongly reduced nebular environments where enstatite chondrites and Earth formed<sup>33</sup>. Multiple generations of oldhamite are present in unequilibrated enstatite chondrites, probably representing condensation in different locations<sup>33</sup>. This indicates that oldhamite was migrating during ongoing mixing processes and solar outflow activities in the inner protoplanetary disk.

Oldhamites have superchondritic Sm/Nd ratios with Sm and Nd abundances of a few to tens of parts per million<sup>33</sup>. Only 0.15 wt% to 0.3 wt% of oldhamite is needed in a mix with bulk enstatite chondrites to reach  $^{147}\text{Sm}/^{144}\text{Nd} = 0.20079 \pm 0.00058$  (Fig. 3a). This results in materials with 8% more Nd than in enstatite chondrites (Fig. 3b) and has little to no effect on other elemental budgets in the materials that form the Earth–Moon system. For U and Th, oldhamite has chondritic concentrations such that a small excess of this material will not significantly affect Earth's heat budget<sup>33</sup>. Adding olivine into the mix with oldhamite

with enstatite chondrites to account for its proposed enriched in Earth–Moon precursor materials<sup>31</sup> does not significantly affect the models for Sm and Nd (Fig. 3a,b).

These results indicate that inhomogeneous distribution of oldhamite or a similar rare-earth-element-rich component with superchondritic Sm/Nd in the inner protoplanetary disk where enstatite chondrites and the Earth–Moon system formed can explain their differences in Sm/Nd ratios. This scenario is attractive as it is consistent with early mixing in the early protoplanetary disk that explains other differences including olivine enrichment in Earth relative to enstatite chondrites<sup>30,31</sup>. Such a scenario also explains the small s-process isotope differences between the Earth–Moon system and enstatite chondrites resulting from pre-solar grain sorting. Finally, it explains an Earth–Moon system with an initial  $\mu^{142}\text{Nd} = -7.3 \pm 1.6$  evolving to  $\mu^{142}\text{Nd} = 0.0 \pm 1.1$  with a Sm/Nd ratio that results in a modest difference of  $\epsilon^{143}\text{Nd} = +2.8 \pm 0.3$  compared with the present-day  $\epsilon^{143}\text{Nd} = 0$  for CHUR.

## Online content

Any methods, additional references, Nature Research reporting summaries, source data, extended data, supplementary information, acknowledgements, peer review information; details of author contributions and competing interests; and statements of data and code availability are available at <https://doi.org/10.1038/s41586-022-05265-0>.

- Burkhardt, C. et al. A nucleosynthetic origin for the Earth's anomalous  $^{142}\text{Nd}$  composition. *Nature* **537**, 394–398 (2016).
- Bouvier, A. & Boyet, M. Primitive Solar System materials and Earth share a common initial  $^{142}\text{Nd}$  abundance. *Nature* **537**, 399–402 (2016).
- McLeod, C. L., Brandon, A. D. & Armitage, R. M. Constraints on the formation age and evolution of the Moon from  $^{142}\text{Nd}$ – $^{143}\text{Nd}$  systematics of Apollo 12 basalts. *Earth Planet. Sci. Lett.* **396**, 179–189 (2014).
- Trinquier, A. et al. Origin of nucleosynthetic isotope heterogeneity in the solar protoplanetary disk. *Science* **324**, 374–376 (2009).
- Warren, P. H. Stable-isotopic anomalies and the accretionary assemblage of the Earth and Mars: a subordinate role for carbonaceous chondrites. *Earth Planet. Sci. Lett.* **311**, 93–100 (2011).
- Kruijer, T. S., Burkhardt, C., Budde, G. & Kleine, T. Age of Jupiter inferred from the distinct genetics and formation times of meteorites. *Proc. Natl Acad. Sci. USA* **114**, 6712–6716 (2017).
- Bouvier, A., Vervoort, J. D. & Patchett, P. J. The Lu–Hf and Sm–Nd isotopic composition of CHUR: constraints from unequilibrated chondrites and implications for the bulk composition of terrestrial planets. *Earth Planet. Sci. Lett.* **273**, 48–57 (2008).
- Boyet, M. et al. Enstatite chondrites EL3 as building blocks for the Earth: the debate over the  $^{146}\text{Sm}$ – $^{142}\text{Nd}$  systematics. *Earth Planet. Sci. Lett.* **488**, 68–78 (2018).
- Brennecka, G. A., Borg, L. E. & Wadhwa, M. Evidence for supernova injection into the solar nebula and the decoupling of r-process nucleosynthesis. *Proc. Natl Acad. Sci. USA* **110**, 17241–17246 (2013).
- Arlandini, C., Käppeler, F. & Wisshak, K. Neutron capture in low-mass asymptotic giant branch stars: cross sections and abundance signatures. *Astrophys. J.* **525**, 886–900 (1999).
- Hoppe, P. & Ott, U. Mainstream silicon carbide grains from meteorites. *AIP Conf. Proc.* **402**, 27–58 (1997).
- Qin, L. P., Carlson, R. W. & Alexander, C. M. O. Correlated nucleosynthetic isotopic variability in Cr, Sr, Ba, Sm, Nd and Hf in Murchison and QUE 97008. *Geochim. Cosmochim. Acta* **75**, 7806–7828 (2011).
- Sprung, P., Kleine, T. & Scherer, E. E. Isotopic evidence for chondritic Lu/Hf and Sm/Nd of the Moon. *Earth Planet. Sci. Lett.* **380**, 77–87 (2013).
- Lugmair, G. W. & Shukolyukov, A. Early Solar System timescales according to  $^{53}\text{Mn}$ – $^{53}\text{Cr}$  systematics. *Geochim. Cosmochim. Acta* **62**, 2863–2886 (1998).
- Zhang, J., Dauphas, N., Davis, A. M., Leya, I. & Fedkin, A. The proto-Earth as a significant source of lunar material. *Nat. Geosci.* **5**, 251–255 (2012).
- Wang, K. & Jacobsen, S. B. Potassium isotopic evidence for a high-energy giant impact origin of the Moon. *Nature* **538**, 487–490 (2016).
- Murphy, D. T., Brandon, A. D., Debaille, V., Burgess, R. & Ballentine, C. In search of a hidden long-term isolated sub-chondritic  $^{142}\text{Nd}/^{144}\text{Nd}$  reservoir in the deep mantle: implications for the Nd isotope systematics of the Earth. *Geochim. Cosmochim. Acta* **74**, 738–750 (2010).
- Lock, S. J. et al. The origin of the Moon within a terrestrial synestia. *J. Geophys. Res.* **123**, 910–951 (2018).
- Nielsen, S. G., Bekaert, D. B. & Auro, M. Isotopic evidence for the formation of the Moon in a canonical giant impact. *Nat. Commun.* **12**, 1817 (2021).
- Thiemens, M. M., Sprung, P., Fonseca, R. O., Leitzke, F. P. & Münker, C. Early Moon formation inferred from hafnium–tungsten systematics. *Nat. Geosci.* **12**, 696–700 (2019).
- Boyet, M. & Carlson, R. W.  $^{142}\text{Nd}$  evidence for early ( $>4.53$  Ga) global differentiation of the silicate Earth. *Science* **309**, 576–581 (2005).
- Boyet, M. & Carlson, R. W. A new geochemical model for the Earth's mantle inferred from  $^{146}\text{Sm}$ – $^{142}\text{Nd}$  systematics. *Earth Planet. Sci. Lett.* **250**, 254–268 (2006).

23. Bennett, V. C., Brandon, A. D. & Nutman, A. P. Hadean mantle dynamics from coupled 142–143 neodymium isotopes in Eoarchean rocks. *Science* **318**, 1907–1910 (2007).
24. Hyung, E. & Jacobsen, S. B. The  $^{142}\text{Nd}/^{144}\text{Nd}$  variations in mantle-derived rocks provide constraints on the stirring rate of the mantle from the Hadean to the present. *Proc. Natl Acad. Sci. USA* **117**, 14738–14744 (2020).
25. Peters, B. J., Carlson, R. W., Day, J. M. D. & Horan, M. F. Hadean silicate differentiation preserved by anomalous  $^{142}\text{Nd}/^{144}\text{Nd}$  ratios in the Reunion hotspot source. *Nature* **555**, 89–93 (2018).
26. O'Neill, H. S. C. & Palme, H. Collisional erosion and the non-chondritic composition of the terrestrial planets. *Phil. Trans. R. Soc. A* **366**, 4205–4238 (2008).
27. Allibert, L., Charnoz, S., Siebert, J., Jacobson, S. A. & Raymond, S. N. Quantitative estimates of impact induced crustal erosion during accretion and its influence on the Sm/Nd ratio of the Earth. *Icarus* **363**, 114412 (2021).
28. Zindler, A. & Hart, S. Chemical geodynamics. *Annu. Rev. Earth Planet. Sci. Lett.* **14**, 493–571 (1986).
29. Campbell, I. H. & O'Neill, H. S. C. Evidence against a chondritic Earth. *Nature* **483**, 553–558 (2012).
30. Miyazaki, Y. & Korenaga, J. Dynamic evolution of major element chemistry in protoplanetary disks and its implications for Earth–enstatite chondrite connection. *Icarus* **361**, 114368 (2021).
31. Johansen, A. et al. A pebble accretion model for the formation of the terrestrial planets in the Solar System. *Sci. Adv.* **7**, eabc0444 (2021).
32. Jacquet, E., Alard, O. & Gounelle, M. The formation conditions of enstatite chondrites: insights from trace element geochemistry of olivine-bearing chondrules in Sahara 97096 (EH3). *Meteorit. Planet. Sci.* **50**, 1624–1642 (2015).
33. Gannoun, A., Boyet, M., El Goresy, A. & Devouard, G. REE and actinide microdistribution in Sahara 97072 and ALHA77295 EH3 chondrites: a combined cosmochemical and petrologic investigation. *Geochim. Cosmochim. Acta* **75**, 3269–3289 (2011).
34. Boyet, M. & Gannoun, A. Nucleosynthetic Nd isotope anomalies in primitive enstatite chondrites. *Geochim. Cosmochim. Acta* **121**, 652–666 (2013).

**Publisher's note** Springer Nature remains neutral with regard to jurisdictional claims in published maps and institutional affiliations.

Springer Nature or its licensor holds exclusive rights to this article under a publishing agreement with the author(s) or other rightsholder(s); author self-archiving of the accepted manuscript version of this article is solely governed by the terms of such publishing agreement and applicable law.

© The Author(s), under exclusive licence to Springer Nature Limited 2022



## Methods

### Sample preparation

Fractions of 1 g to 2 g of the enstatite chondrite samples were processed and measured at two facilities: the University of Houston (UH) and Freie University of Berlin (Berlin). Samples analysed at UH were crushed into fine powders with a ceramic mortar and pestle that is dedicated to chondritic meteorites. The mortar and pestle were thoroughly cleaned with silica sand and ethanol between each use, then rinsed in ultrapure water. Samples were combined with 2.5 ml twice-distilled concentrated nitric acid (HNO<sub>3</sub>) and 7.5 ml of Optima concentrated hydrofluoric acid in polytetrafluoroethylene inserts. These were placed into stainless-steel jackets (Parr bombs) and heated at 170 °C, under pressure, for one week. Following this initial digestion, each sample was taken to dryness. Samples were further digested in Teflon beakers on a hot plate. Each sample was combined with 2 ml twice-distilled concentrated HNO<sub>3</sub> at 120 °C for 12 h, then taken to dryness. These samples were then combined with 1 ml concentrated hydrochloric acid (HCl) at 80 °C for 12 h, then taken to dryness. This step was repeated an additional time. For each sample, this resulted in a small final residue.

Samples analysed at the Berlin laboratory were digested, purified and measured for their Nd isotope composition. Samples were first crushed into a fine powder. The method used a strongly oxidative dissolution protocol with a sodium hydroxide and water (NaOH·H<sub>2</sub>O) solution that was molten at 400 °C and contained in a graphite crucible. This ensured that acid-resistant grains were quantitatively brought into solution. This molten solution was poured over a sample/sodium peroxide (Na<sub>2</sub>O<sub>2</sub>) mixture in a separate graphite crucible with a sample-to-Na<sub>2</sub>O<sub>2</sub>-to-NaOH ratio of 1:6:3. This mixture was then molten at 650 °C for 15 min and then swirled to ensure complete sample dissolution. This step was repeated twice. After the crucible cooled, ultrapure water was added in small quantities to decompose the melt cake. The resulting hydroxide precipitates were then centrifuged and washed with ultrapure water five times. They were then dissolved in 6 M HCl. At this stage, a clear solution was obtained. Occasionally, small nuggets of metal remained. These were attacked separately with concentrated HNO<sub>3</sub>, and the resulting solutions were combined with the main cuts.

For the same samples, the Nd isotope compositions from both laboratories (with the exception of <sup>148</sup>Nd as discussed below) are reproducible within error. Hence, both digestion techniques accessed the same Nd in these samples and both digestion techniques are consistent with those used in previous studies cited here and used in this paper.

### Chemical procedures for Sm and Nd isotope composition measurements

At UH, the rare-earth elements (REEs), including Nd and Sm, were purified through cation exchange chromatography using Bio-Rad AG 50W-X8 resin and distilled HCl. The REE cuts were purified of cerium (Ce) as <sup>142</sup>Ce is a major mass interference with <sup>142</sup>Nd. Ce in the REE cuts was oxidized from +3 to +4 using sodium bromate (NaBrO<sub>3</sub>) in a HNO<sub>3</sub> solution. These solutions were eluted through Ln-Spec resin using NaBrO<sub>3</sub> + HNO<sub>3</sub> while oxidized Ce<sup>+4</sup> remained complexed with the Ln-Spec resin<sup>35</sup>. Sodium introduced from the NaBrO<sub>3</sub> was removed by eluting the samples through Bio-Rad AG 50W-X8 resin columns with ultrapure HCl. Nd and Sm were purified through an Ln-Spec column using 0.25N and 0.4N distilled HCl, respectively. This step was repeated to purify Sm. Purified Sm and Nd cuts were loaded onto outgassed rhenium filaments with phosphoric acid (H<sub>3</sub>PO<sub>4</sub>). These loaded filaments were placed in a double-filament configuration as the evaporation filament, using an additional outgassed rhenium filament as the ionization filament.

At Berlin, the REEs were purified through 10-ml columns using Bio-Rad AG 50W-X8 resin and distilled HCl. Nd and Sm were initially separated on Ln-Spec columns. The Nd and Sm fractions were then cleaned in quartz glass columns using 0.21 M alpha-hydroxyisobutyric

acid (α-HIBA) at pH 4.60. The samples were subsequently loaded onto small 2-ml cation columns to wash off residual organics. Finally, all Nd and Sm cuts were again loaded onto the Ln-Spec columns to obtain pure final separates. Purified Nd cuts were loaded onto outgassed rhenium filaments and placed in a double-filament configuration as the evaporation filament, using an additional outgassed rhenium filament as the ionization filament.

### Procedures for Sm and Nd concentration measurements

At UH, for each sample, 5–10 mg of material was powdered and spiked with a mixed <sup>149</sup>Sm–<sup>150</sup>Nd spike. At Berlin, 50 mg of material was powdered and spiked with a mixed <sup>149</sup>Sm–<sup>148</sup>Nd spike. Samples at each laboratory were then prepared following the procedure of the non-spiked samples.

### Sm and Nd isotope measurements by thermal ionization mass spectrometry

The Nd isotopes of samples and standards analysed at the UH laboratory were measured on a ThermoScientific Triton-Plus thermal ionization mass spectrometer using the three-line multistatic cup configuration. This configuration allowed for <sup>148</sup>Nd to be measured across three Faraday cups and <sup>150</sup>Nd to be measured across two cups. The Nd isotopes of samples analysed at the Berlin laboratory were measured on a ThermoScientific Triton thermal ionization mass spectrometer using the three-line multistatic technique outlined in ref. <sup>36</sup>. All Nd isotope data are given in μNd notation, as parts-per-million deviations from the average Nd isotope composition of the measured JNdi standard. All Nd isotope data from both laboratories were internally normalized to a <sup>146</sup>Nd/<sup>144</sup>Nd ratio of 0.7219 and corrected for mass bias using the exponential law. Samples from Berlin were measured relative to an AMES metal Nd standard obtained from Ames Metal Products, which was also used at UH (Supplementary Table 2). Their μNd values are renormalized for direct comparison with JNdi normalization as discussed in the next section.

### Renormalization of AMES normalized samples to JNdi standards

Samples in this study were processed and analysed in three separate campaigns. The standards for each campaign are given in Supplementary Table 2. Samples measured in Berlin were normalized to the AMES metal Nd standard at the time of measurement and were renormalized to the JNdi standard using the following:

$$\mu^i\text{Nd}_{\text{JNdi norm}} = \left( \frac{\left( \left( {}^i\text{Nd}/{}^{144}\text{Nd} \right)_{\text{sample}} \frac{({}^i\text{Nd}/{}^{144}\text{Nd})_{\text{JNdi-UH}}}{({}^i\text{Nd}/{}^{144}\text{Nd})_{\text{AMES-UH}}} \right)}{({}^i\text{Nd}/{}^{144}\text{Nd})_{\text{AMES-Berlin}}} - 1 \right) \times 10^6$$

where  $({}^i\text{Nd}/{}^{144}\text{Nd})_{\text{AMES-UH}}$  is the average AMES metal Nd ratio measured at the UH facility,  $({}^i\text{Nd}/{}^{144}\text{Nd})_{\text{JNdi-UH}}$  is the average JNdi Nd ratio measured at the UH facility concurrent to the measured AMES metal standards and  $({}^i\text{Nd}/{}^{144}\text{Nd})_{\text{AMES-Berlin}}$  is the average AMES Nd ratio measured at the Berlin facility, used to normalized samples at the time of measurement.

### Correction of radiogenic <sup>142</sup>Nd

A sample's measured <sup>142</sup>Nd has two distinct components: nucleosynthetic <sup>142</sup>Nd and radiogenic <sup>142</sup>Nd. The <sup>142</sup>Nd/<sup>144</sup>Nd ratios are affected by early fractionation of Sm/Nd because of the decay of <sup>146</sup>Sm decay to <sup>142</sup>Nd with a half-life (*t*<sub>1/2</sub>) = 103 Myr (refs. <sup>37–39</sup>). The short-lived <sup>146</sup>Sm is thus effectively decayed away by approximately 500 Myr after Solar System formation, such that no detectable change to <sup>142</sup>Nd/<sup>144</sup>Nd ratios in a sample occurs from this process after this time. To compare the starting <sup>142</sup>Nd/<sup>144</sup>Nd ratios of chondritic materials at a 4.568 Ga formation time, ingrowth of radiogenic <sup>142</sup>Nd from radioactive <sup>146</sup>Sm is corrected for.

All samples were corrected using the integrated <sup>147</sup>Sm/<sup>144</sup>Nd method, as measured <sup>147</sup>Sm/<sup>144</sup>Nd ratios are more susceptible to changes from

terrestrial weathering, and recent changes in Sm/Nd ratios will not be recorded in the integrated  $^{147}\text{Sm}/^{144}\text{Nd}$  (refs. <sup>1,9</sup>). This correction method assumes that the initial  $^{143}\text{Nd}/^{144}\text{Nd}$  values for all samples is 0.506686 (the value of CHUR at time ( $t$ ) =  $4.568 \times 10^9$  yr) and a chondritic  $^{147}\text{Sm}/^{144}\text{Nd}$  value of 0.1960 (ref. <sup>7</sup>) and an initial Solar System  $^{146}\text{Sm}/^{144}\text{Sm}$  value of 0.0085 (ref. <sup>40</sup>). Using these values and a decay constant ( $\lambda$ ) =  $6.54 \times 10^{-12}$  yr, the following equations were used to correct for radiogenic  $^{142}\text{Nd}$ :

$$\begin{aligned} \left( \frac{^{143}\text{Nd}}{^{144}\text{Nd}} \right)_{\text{today}}^{\text{CHUR}} &= \left( \frac{^{143}\text{Nd}}{^{144}\text{Nd}} \right)_{4.568 \text{ Ga}} + \left( \frac{^{147}\text{Sm}}{^{144}\text{Nd}} \right) (e^{\lambda t} - 1) \left( \frac{^{142}\text{Nd}}{^{144}\text{Nd}} \right)_{\text{corrected}} \\ &= \left( \frac{^{142}\text{Nd}}{^{144}\text{Nd}} \right)_{\text{measured}} + \left( \frac{\left( \frac{^{146}\text{Sm}}{^{144}\text{Nd}} \right)_{\text{CHUR}}}{\left( \frac{^{147}\text{Sm}}{^{144}\text{Sm}} \right)} \times \left( \frac{^{147}\text{Sm}}{^{144}\text{Nd}} \right)_{\text{sample}} \right) \\ &\quad - \left( \frac{\left( \frac{^{146}\text{Sm}}{^{144}\text{Nd}} \right)_{\text{CHUR}}}{\left( \frac{^{147}\text{Sm}}{^{144}\text{Sm}} \right)} \times \left( \frac{^{147}\text{Sm}}{^{144}\text{Nd}} \right)_{4.568 \text{ Ga}}^{\text{CHUR}} \right) (e^{\lambda t} - 1) \end{aligned}$$

The corrected measured and calculated  $^{147}\text{Sm}/^{144}\text{Nd}$ , measured  $^{143}\text{Nd}/^{144}\text{Nd}$ ,  $\mu^{142}\text{Nd}$  and the corrected values using this method for the samples measured in this study, denoted as  $^{142}\text{Nd}_{\text{corr}}$  in the paper, are listed in Supplementary Table 3.

## Calculating group averages and data filtering

All samples compiled from the literature and the samples in this study (Supplementary Table 1) were normalized to the JNdi standard measured in each study for direct comparison of  $\mu$  values of each isotope. The JNdi values for  $^{142}\text{Nd}/^{144}\text{Nd}$ ,  $^{145}\text{Nd}/^{144}\text{Nd}$ ,  $^{148}\text{Nd}/^{144}\text{Nd}$  and  $^{150}\text{Nd}/^{144}\text{Nd}$  are the same as modern terrestrial mantle-derived samples and thus are considered to represent the present-day bulk Earth<sup>1</sup>.

To calculate the enstatite chondrite, ordinary chondrite, carbonaceous chondrite, Allende and CAI group averages, the data were filtered as follows.

Data for 1 ordinary chondrite and 2 carbonaceous chondrites from ref. <sup>41</sup> were not used because the JNdi standard was not measured and their standard was not used at the other labs where direct comparisons between standards can be made. This is particularly important for  $^{148}\text{Nd}/^{144}\text{Nd}$  and  $^{150}\text{Nd}/^{144}\text{Nd}$  because the different terrestrial Nd standard can have different values for these ratios<sup>21,42,43</sup>.

The bulk chondrite samples Blithfield (EL6) and Atlanta (EL6) from ref. <sup>1</sup>, Blithfield from this study, Adrian (H4), NWA 2090 (CO3), Kainsaz (CO3) and Tagish Lake (C2) from refs. <sup>44,45</sup>, and Kota Kota (EH3) from ref. <sup>46</sup> reflect disturbances in their Sm/Nd systematics, probably by late-stage impacts, so were not included. The analyses of Blithfield in this study also found superchondritic  $^{143}\text{Nd}/^{144}\text{Nd}$  ratios (as high as  $\epsilon^{143}\text{Nd} = 27.8$ ), indicating a later  $^{147}\text{Sm}/^{144}\text{Nd}$  fractionation event relative to the initial parent-body processing. These samples were removed from further consideration in the discussion that follows. Sample NWA 8522 (EL6) from ref. <sup>47</sup> was removed owing to superchondritic  $^{143}\text{Nd}/^{144}\text{Nd}$  ( $\epsilon^{143}\text{Nd} = 8.2$ ), which they interpreted to be a result of weathering of an accessory mineral phase that was depleted in Sm.

For CAI group averages, only whole CAI fractions from Allende were used. This is because the CAI group average is used to correct the Allende bulk fractions for the CAI component following ref. <sup>1</sup> (Supplementary Table 5). Hence CAI mineral separate data from ref. <sup>39</sup> are not used as these have both subchondritic and superchondritic  $^{147}\text{Sm}/^{144}\text{Nd}$  ratios and indicate that these fractions are not representative of a bulk CAI but instead specific to the purified minerals within each fraction<sup>39</sup>. Two CAI samples from Allende were measured by ref. <sup>2</sup>. These have distinct Nd isotopic compositions for  $^{145}\text{Nd}$ ,  $^{148}\text{Nd}$  and  $^{150}\text{Nd}$ , and higher

$^{147}\text{Sm}/^{144}\text{Nd}$  ratios, compared with the 12 samples measured elsewhere<sup>1,9</sup> (Supplementary Table 1). These two CAIs probably represent sourcing from a different location and/or process and it remains to be examined how representative of Allende CAIs these are. Hence, they were not included in the group average for CAIs.

Within the enstatite and carbonaceous chondrite datasets, out of the 70 measured bulk fractions considered for their group averages, 7 samples had  $\mu^{145}\text{Nd}$  values (from refs. <sup>44–46</sup>) that were far removed from the rest of the values and were considered as outliers. Likewise, for  $\mu^{148}\text{Nd}$  in two enstatite chondrite measurements (from ref. <sup>46</sup> and this study UH) were far removed from the rest of the values and were considered as outliers. These were not used in their respective group averages (Supplementary Table 1).

Two different analytical issues can potentially cause artefacts, in particular for  $^{150}\text{Nd}$ . The first is non-exponential mass fractionation from domain mixing of Nd on the filament while performing the measurements<sup>48</sup>. The isotope  $^{150}\text{Nd}$  is the smallest in abundance (0.056) among Nd and is 4 and 6 mass units, respectively, from the normalizing isotopes  $^{146}\text{Nd}$  and  $^{144}\text{Nd}$ , such that any analytical artefact is therefore exacerbated on mass  $^{150}\text{Nd}$  relative to the other Nd isotopes and will hence show up on this mass first. A second issue is fractionation induced by laboratory-scale chemical exchange<sup>49</sup>. Both issues result in anomalously elevated  $\mu^{150}\text{Nd}$  and, as such, is the first indication that either of these have occurred. Although this can be hard to identify, to proceed with caution, elevated  $\mu^{150}\text{Nd}$  data that were consistent with either of these anomalous fractionation processes were systematically removed from all group averages (Supplementary Table 1). This resulted in removing 18 elevated  $\mu^{150}\text{Nd}$  values from the 127 measurements used to calculate the group averages.

Finally, the  $\mu^{148}\text{Nd}$  values for some of the samples measured at the Berlin laboratory show erroneously high values. This was only discovered after completion of the analytical campaign. The  $\mu^{148}\text{Nd}$  measurements for these samples are always higher than their respective  $\mu^{150}\text{Nd}$  values, despite no proportional differences in other s-process isotopes to explain this ratio (Supplementary Table 2). Of particular note is the Earth komatiite measured in this suite and listed in Table 1 and Supplementary Table 2), which shows an anomalously high  $\mu^{148}\text{Nd}$  value of 120, which is higher than the anomalously high values for the enstatite chondrites measured at the Berlin facility. As all terrestrial samples should have  $\mu^{148}\text{Nd}$  values within uncertainty of 0, this is consistent with having the  $^{148}\text{Nd}$  spike used at the Berlin facility as the most likely cause of these anomalies. This means that in the likely situation that the elevated  $^{148}\text{Nd}$  comes from the  $^{148}\text{Nd}$  spike, then cross-contamination, unclean beakers, improperly cleaned columns or a combination of all the above is the culprit. However, the rest of the Nd isotope data from Berlin is comparable to the other datasets for enstatite chondrites from UH and those in Supplementary Table 1. Because of this issue, we disregard the nine Berlin  $\mu^{148}\text{Nd}$  measurements for enstatite chondrites and two Allende bulk fractions, even though some of these may be accurate within uncertainties of the measurements. We prefer to err on the side of caution for this issue. The isotope abundances of the Berlin  $^{148}\text{Nd}$  spike is as follows: 0.01223  $^{142}\text{Nd}$ , 0.006189  $^{143}\text{Nd}$ , 0.013062  $^{144}\text{Nd}$ , 0.005608  $^{145}\text{Nd}$ , 0.017551  $^{146}\text{Nd}$ , 0.932828  $^{148}\text{Nd}$  and 0.012532  $^{150}\text{Nd}$ . Thus even with an anomalous value in  $^{148}\text{Nd}$  that is 100 ppm high (the Berlin enstatite chondrite samples have  $\mu^{148}\text{Nd} \leq 69.6$ , potentially a 69.6-ppm excess), and owing to the fact that 93.28% of the spike is  $^{148}\text{Nd}$  with the rest of the Nd isotopes dilute in abundance, the effects on the other Nd isotopes is less than 1 ppm and thus did not result in erroneous values. This is born out for the komatiite measurement with  $\mu^{142}\text{Nd} = 1.1 \pm 3.1$ ,  $\mu^{145}\text{Nd} = -0.78 \pm 2.4$ ,  $\mu^{148}\text{Nd} = 120.2 \pm 5.6$  and  $\mu^{150}\text{Nd} = 3.1 \pm 10.3$  that show the correct terrestrial values within the uncertainties of the measurement. As the  $\mu^{148}\text{Nd}$  values for the Berlin chondrite samples are +12–73 and lower than those for the komatiite measurement (Supplementary Table 2), their spike contamination, where present, is also less and negligible.



## Confidence intervals

CI for group averages were calculated using the following:

$$CI = \bar{X} \pm t_{95} \left( \frac{s_{\bar{X}}}{\sqrt{n}} \right)$$

where CI is the 95% CI,  $\bar{X}$  is the group average,  $t_{95}$  is the  $t$ -value for a two-tailed test with an  $\alpha$  value of 0.05,  $s_{\bar{X}}$  is the standard deviation of the group population and  $n$  is the population number. The CI gives the range that contains a population's average with a 95% level of confidence. Whereas standard deviations factor in analytical biases, measurement uncertainties and the variability of inter-group sample isotope compositions (that is, a single sample is not representative of the bulk parent body), CIs determine the variance of the isotope compositional average of the group, which we assume to represent the bulk parent body. Using the CIs here for each chondrite group average follows the approach of previous Nd isotope studies on chondrites and their fractions<sup>19</sup>. The final values and uncertainties for the group averages using this computational method are listed in Supplementary Tables 1 and 4.

## Allende CAI-free composition mass-balance calculations

To characterize the Nd composition of the non-CAI material in Allende, an isotopic mass balance was performed using the following<sup>1</sup>:

$$\mu^{i}\text{Nd}_{\text{CAI-free}} = \frac{\mu^{i}\text{Nd}_{\text{Allende}}[\text{Nd}_{\text{Allende}}] - (1 - X)\mu^{i}\text{Nd}_{\text{CAI}}[\text{Nd}_{\text{CAI}}]}{[\text{Nd}_{\text{Allende}}] - (1 - X)[\text{Nd}_{\text{CAI}}]}$$

where  $\text{Nd}_{\text{Allende}}$  is the mean concentration of Allende CV3,  $\mu^{i}\text{Nd}_{\text{Allende}}$  is the isotope composition of 12 measurements of Allende (refs. <sup>1,21,42,44</sup> and this study),  $\text{Nd}_{\text{CAI}}$  is the mean concentration of CAIs<sup>50</sup>,  $\mu^{i}\text{Nd}_{\text{Allende}}$  is the weighted mean isotope composition of 12 measurements of Allende CAIs<sup>19</sup>, and  $X$  is the fraction of non-CAI material in Allende (0.97)<sup>50</sup> listed in Source Data Table 1. The results of these mass-balance calculations are summarized in Supplementary Table 5. This method is the same used in ref. <sup>1</sup>, and thus provides a direct comparison between this paper and the inclusion of our data here.

## Assessing uncertainty on the present-day accessible Earth Nd isotope composition

Two approaches assess uncertainty on averages of related groups of analyses of high-precision Nd isotope measurements. One approach uses  $\pm 2$  s.d. (or  $2\sigma$ , 2 times the standard deviation of the mean)<sup>8,36,49</sup>. The second approach uses uncertainty calculated at the 95% CI shown above<sup>19</sup>. Uncertainties using this approach are a factor of one to three times lower than using  $\pm 2\sigma$  depending on the number of samples, which are factored in the calculation by the square root of  $n$  (see above). The 95% CI uncertainties are valid for assessing the variability of the data we examine here because these averages are considered to represent the bulk compositions of parent bodies in the Solar System. More analyses of each provides a more accurate average for each body<sup>19</sup>. For example, enstatite chondrite data reflect the average composition of the enstatite chondrite parent body (or bodies). Uncertainty is a consequence of s-process and r-process variability between samples, measurement error and, possibly, chemical processing (see below). For consistency and direct comparison with the average of accessible Earth/bulk silicate Earth, we hence use the 95% CI to assess uncertainty. For the terrestrial materials, the 95% CI and  $\pm 2\sigma$  are listed in Supplementary Table 1 for group averages that are considered in the following assessment.

Here, 3 different datasets are considered to obtain the 95% CI uncertainties on the accessible Earth  $\mu^{142}\text{Nd}$ ,  $\mu^{145}\text{Nd}$ ,  $\mu^{148}\text{Nd}$  and  $\mu^{150}\text{Nd}$ . The first dataset considered is that of ref. <sup>24</sup>, which measured 13 terrestrial samples with ages  $\leq 2$  Ga including modern mid-ocean-ridge basalts. They report only  $^{142}\text{Nd}/^{144}\text{Nd}$  and  $^{143}\text{Nd}/^{144}\text{Nd}$ . These samples have an  $\epsilon^{143}\text{Nd}$  range of  $-23.7$  to  $+12.1$ , and thus are a strong representation of

the Earth's variability in Nd isotope compositions. For  $\mu^{142}\text{Nd}$ , they obtained an average of  $+0.4$  for these samples, and concluded that Earth's accessible, convecting mantle since 2 Ga is well mixed with a  $\pm 2\sigma$  uncertainty of  $\pm 1.7$  ppm, based on their replicate measurements of the JNdi standard. Using the same approach to obtaining averages for the different chondrite groups, these samples give a 95% CI uncertainty of  $\pm 1.0$  for  $\mu^{142}\text{Nd}$ . Another approach is to use the JNdi standard values obtained with the samples measured here (Supplementary Table 2). This is because the average values for JNdi are used for normalization of the chondrite data and hence, is argued to represent the present-day accessible Earth for which the chondrite data are directly compared with. The respective  $\mu\text{Nd}$  values are by definition all zero. Using this approach on 15 measurements of JNdi here, the CI value for  $\mu^{142}\text{Nd}$  is  $\pm 1.1$ , for  $\mu^{145}\text{Nd}$  is  $\pm 0.4$ , for  $\mu^{148}\text{Nd}$  is  $\pm 1.4$  and for  $\mu^{150}\text{Nd}$  is  $3.2$ . Finally, the third approach is to use a set of internally consistent oceanic island basalts. For this, the dataset reported in ref. <sup>17</sup>, for Hawaii, Iceland and Gough Island are used, and the Iceland sample ICE 9a measured here (Supplementary Table 2). The samples studied have a range of  $\epsilon^{143}\text{Nd}$  of  $-1.4$  to  $+8.3$ , and thus are a strong representation of the global ocean-island-basalt Nd compositional variation ( $n = 13$ ). For these ocean island basalts, the 95% CI value for  $\mu^{142}\text{Nd}$  is  $\pm 1.1$ , for  $\mu^{145}\text{Nd}$  is  $\pm 1.6$ , for  $\mu^{148}\text{Nd}$  is  $\pm 2.9$  and for  $\mu^{150}\text{Nd}$  is  $7.9$ , with average values all within 95% CI uncertainties of 0 for the JNdi standard. The CI value of  $\pm 1.1$  for  $\mu^{142}\text{Nd}$  is comparable to that for the ref. <sup>24</sup> samples and for the JNdi standard from this study. However, the  $\mu^{145}\text{Nd}$ ,  $\mu^{148}\text{Nd}$  and  $\mu^{150}\text{Nd}$  CI values for the averages of the ocean island basalts are two to four times larger than those for the JNdi standard measured here. This may reflect nuclear field shifts induced as a result of chemical processing to purify Nd that affect these Nd isotopes more than for  $^{142}\text{Nd}$  (ref. <sup>49</sup>). Also, the ref. <sup>17</sup> data were obtained at the NASA Johnson Space Center in Houston using a multistatic measuring routine on the Triton in the lab of A.B. The values are normalized to an AMES Nd standard. This AMES metal standard is different from the AMES metal standard used at Berlin and UH (as indicated by their  $^{143}\text{Nd}/^{144}\text{Nd}$  ratios), and no JNdi standard was available at that time at the Johnson Space Center. Hence these values are not normalized to JNdi as there is no direct way to compare. The Nd isotope ratio values  $^{142}\text{Nd}/^{144}\text{Nd}$  and  $^{145}\text{Nd}/^{144}\text{Nd}$  for this standard are comparable within uncertainty to those obtained by JNdi here and in other studies. Where the differences may lie is for  $^{148}\text{Nd}/^{144}\text{Nd}$  and  $^{150}\text{Nd}/^{144}\text{Nd}$ , where different AMES metals and other standards could have up to 10-ppm deviations in these ratios relative to JNdi<sup>43</sup>. Nevertheless, the ref. <sup>17</sup> averaged  $\mu\text{Nd}$  values normalized to the AMES metal standard in that study are within  $\pm 2\sigma$  of that for the JNdi standard measured here (Supplementary Tables 1 and 2), and thus, there may be slight inaccuracies of a few parts per million for  $^{148}\text{Nd}/^{144}\text{Nd}$  and  $^{150}\text{Nd}/^{144}\text{Nd}$  averaged ratios and respective absolute  $\mu\text{Nd}$  values for this group because of using this AMES metal standard relative to JNdi for normalization. This may also be part of the reason why the  $\pm \text{CI}$  values are larger for  $\mu^{148}\text{Nd}$  and  $\mu^{150}\text{Nd}$  than for the respective values using JNdi from this study. Hence, because of these issues, we believe that the CI values for JNdi, for which all of the chondrite data are normalized to, represent the most accurate uncertainty on the average for accessible Earth where only measurement errors are present and when directly comparing with chondrite group averages. JNdi is adopted here as best representing the present-day accessible Earth and the accepted normalizing values for Nd isotope ratios.

The CI values for the chondrite groups for  $\mu^{145}\text{Nd}$ ,  $\mu^{148}\text{Nd}$  and  $\mu^{150}\text{Nd}$  may also have increased scatter as a result of chemical processing. Some of this scatter was probably removed using the data filtering techniques discussed above, but possibly not all. However, the average values themselves are accurate within CI uncertainties based on the comparisons between the JNdi standard, and ocean island basalts in Supplementary Table 1 discussed in the previous paragraph, and based on comparisons between the ref. <sup>1</sup> dataset and those from the other labs discussed in the main text (Extended Data Fig. 3).

## Data availability

All data are available at EarthChem<sup>51</sup>. Source data are provided with this paper.

35. Tazoe, H., Obata, H. & Gamo, T. Determination of cerium isotope ratios in geochemical samples using oxidative extraction technique with chelating resin. *J. Anal. At. Spectrom.* **22**, 616–622 (2007).
36. Caro, G., Bourdon, B., Birck, J. L. & Moorbath, S. High-precision <sup>142</sup>Nd/<sup>144</sup>Nd measurements in terrestrial rocks: constraints on the early differentiation of the Earth's mantle. *Geochim. Cosmochim. Acta* **70**, 164–191 (2006).
37. Friedman, A. M. et al. Alpha decay half lives of <sup>148</sup>Gd <sup>150</sup>Gd and <sup>146</sup>Sm. *Radiochim. Acta* **5**, 192–194 (1966).
38. Meissner, F., Schmidt-Ott, W. D. & Ziegeler, L. Half-life and α-ray energy of <sup>146</sup>Sm. *Z. Phys. A* **327**, 171–174 (1987).
39. Marks, N. E., Borg, L. E., Hutcheon, I. D., Jacobsen, B. & Clayton, R. N. Samarium–neodymium chronology and rubidium–strontium systematics of an Allende calcium–aluminum-rich inclusion with implications for <sup>146</sup>Sm half-life. *Earth Planet. Sci. Lett.* **405**, 15–24 (2014).
40. Boyet, M., Carlson, R. W. & Horan, M. Old Sm–Nd ages for cumulate eucrites and redetermination of the solar system initial <sup>146</sup>Sm/<sup>144</sup>Sm ratio. *Earth Planet. Sci. Lett.* **291**, 172–181 (2010).
41. Andreasen, R. & Sharma, M. Solar nebula heterogeneity in p-process samarium and neodymium isotopes. *Science* **314**, 806–809 (2006).
42. Carlson, R. W., Boyet, M. & Horan, M. Chondrite barium, neodymium, and samarium isotopic heterogeneity and early Earth differentiation. *Science* **316**, 1175–1178 (2007).
43. O'Neil, J., Carlson, R. W., Francis, D. & Stevenson, R. K. Response to Comment on “Neodymium-142 evidence for Hadean mafic crust”. *Science* **325**, 267 (2009).
44. Fukai, R. & Yokoyama, T. Neodymium isotope heterogeneity of ordinary and carbonaceous chondrites and the origin of non-chondritic <sup>142</sup>Nd compositions in the Earth. *Earth Planet. Sci. Lett.* **474**, 206–214 (2017).
45. Fukai, R. & Yokoyama, T. Nucleosynthetic Sr–Nd isotope correlations in chondrites: evidence for nebular thermal processing and dust transportation in the early Solar System. *Astrophys. J.* **879**, 79 (2019).
46. Gannoun, A., Boyet, M., Rizo, H. & El Goresy, A. <sup>146</sup>Sm–<sup>142</sup>Nd systematics measured in enstatite chondrites reveals a heterogeneous distribution of <sup>142</sup>Nd in the solar nebula. *Proc. Natl Acad. Sci. USA* **108**, 7693–7697 (2011).
47. Saji, N. S., Wielandt, D., Holst, J. C. & Bizzarro, M. Solar System Nd isotope heterogeneity: insights into nucleosynthetic components and protoplanetary disk evolution. *Geochim. Cosmochim. Acta* **281**, 135–148 (2020).
48. Andreasen, R. & Sharma, M. Fractionation and mixing in a thermal ionization mass spectrometer source: implications and limitations for high-precision Nd isotope analyses. *Int. J. Mass Spectrom.* **285**, 49–57 (2009).
49. Garçon, M. et al. Factors influencing the precision and accuracy of Nd isotope measurements by thermal ionization mass spectrometry. *Chem. Geol.* **476**, 493–514 (2018).
50. Hezel, D. C. & Palme, H. Constraints for chondrule formation from Ca–Al distribution in carbonaceous chondrites. *Earth Planet. Sci. Lett.* **265**, 716–725 (2008). 2008.
51. Johnston, S. et al. Extended Data Files for 'Nd isotope variation between the Earth–Moon system and enstatite chondrites', published in *Nature*, Version 1.0. IEDA <https://doi.org/10.26022/IEDA/112516> (2022).

**Acknowledgements** We thank the NASA Emerging Worlds Program for funding via award #NNX16AI28G and #8ONSSC21KO275, and DFG for funding via award RA1797-1. A visit of A.B. at Freie Universität Berlin was funded by DFG CRC-TRR 170 (Project-ID 263649064). We thank M. Feth and K. Hammerschmidt for assistance and discussions. We thank the Smithsonian Institution in Washington, DC, USA, and the Antarctic Meteorite Collection at the NASA Johnson Space Center in Houston, TX, USA, for samples. This is TRR 170 publication no. 168.

**Author contributions** S.J. performed lab work and measurements and took the lead in writing the paper and interpretation. A.B. conceived the project, supervised all work at University of Houston, performed lab work and measurements. C.M. performed lab work and measurements. K.R. performed lab work and measurements. H.B. supervised all work at Freie University. P.C. provided guidance for the study. All authors contributed to interpretation and editing the manuscript.

**Competing interests** The authors declare no competing interests.

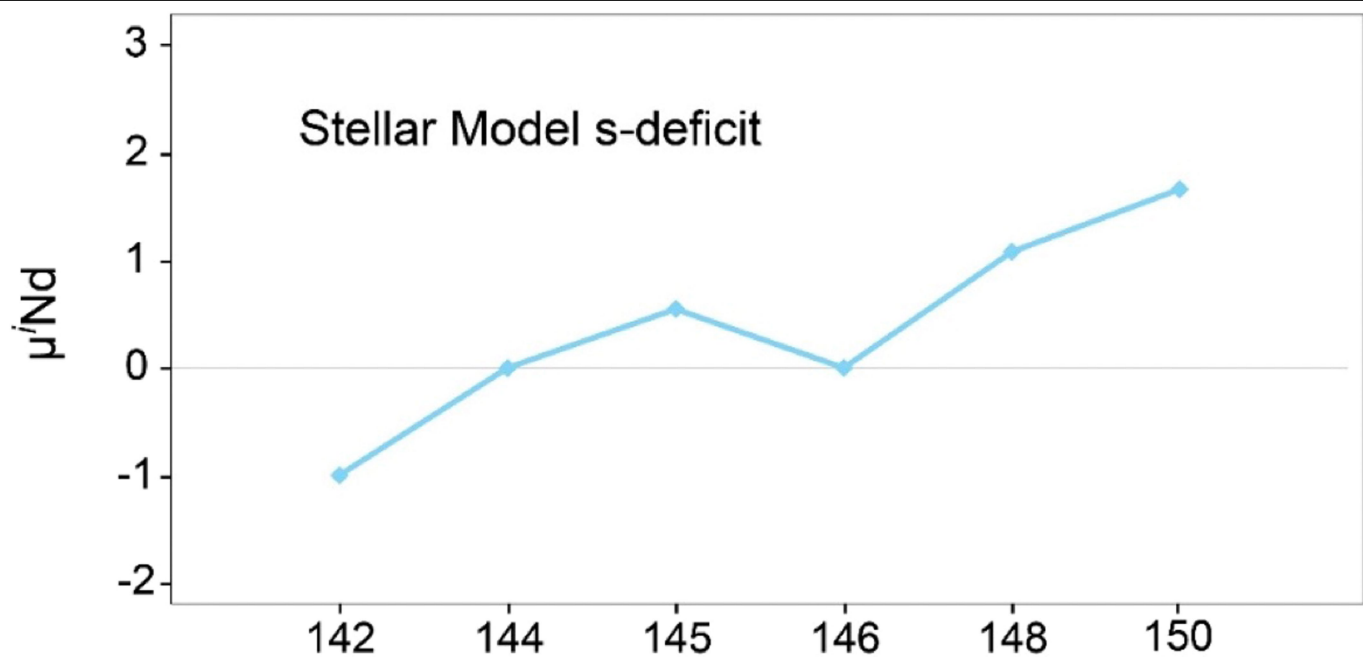
### Additional information

**Supplementary information** The online version contains supplementary material available at <https://doi.org/10.1038/s41586-022-05265-0>.

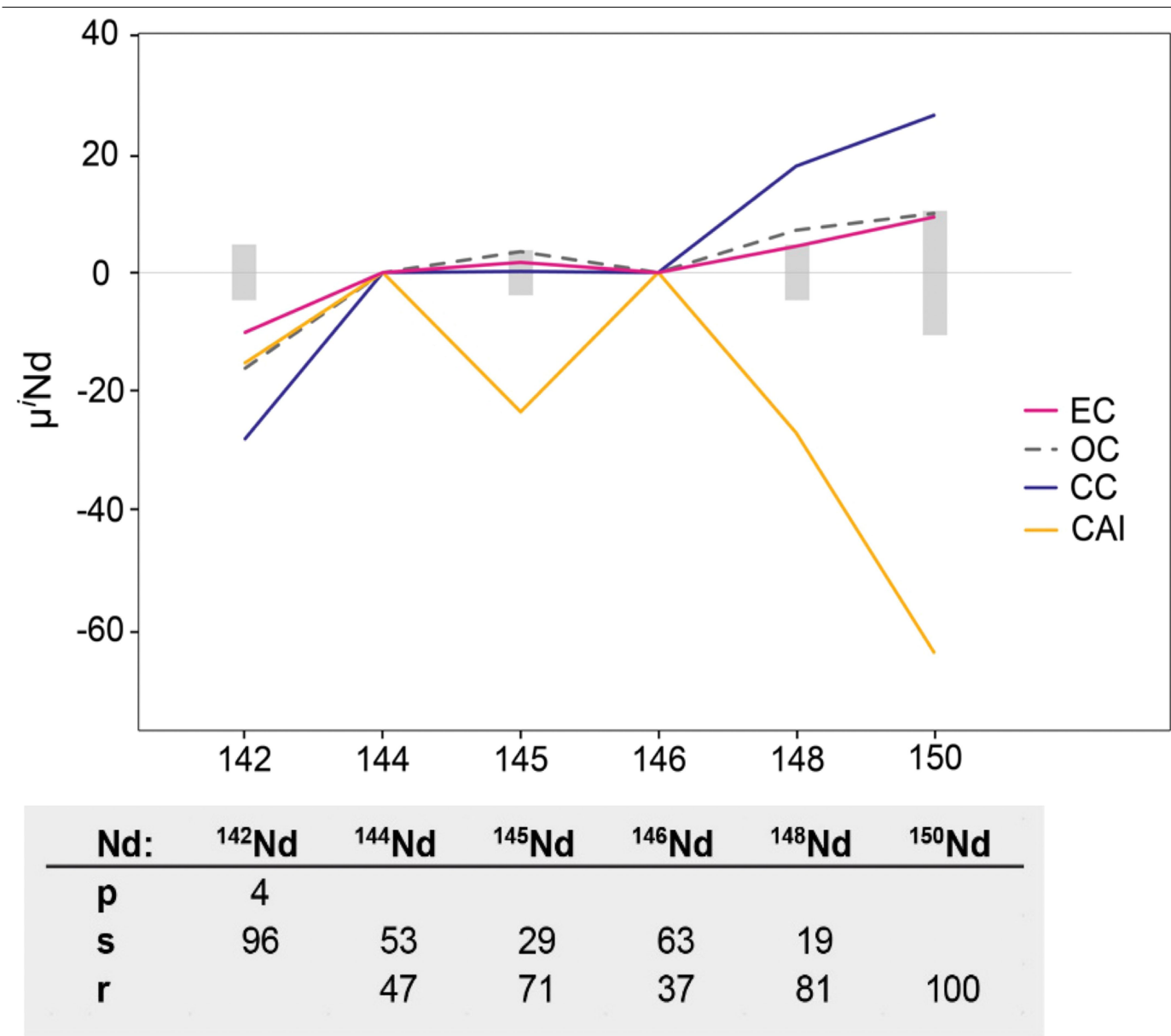
**Correspondence and requests for materials** should be addressed to Alan Brandon.

**Peer review information** *Nature* thanks the anonymous reviewers for their contribution to the peer review of this work.

**Reprints and permissions information** is available at <http://www.nature.com/reprints>.

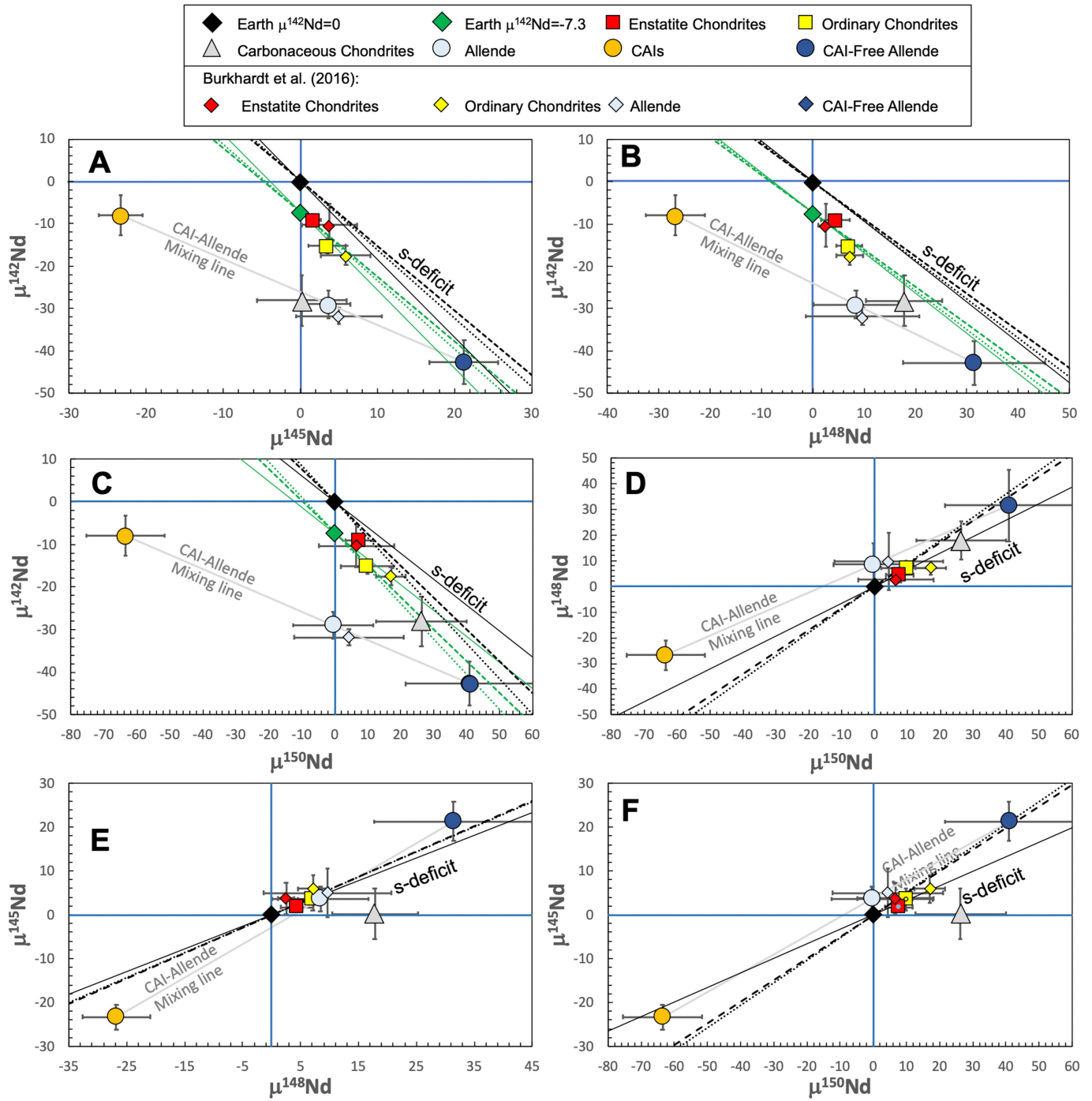


**Extended Data Fig. 1 | Nucleosynthetic anomaly patterns for Nd.** The expected s-deficit Nd anomalies when using stellar model abundances and an internal  $^{146}\text{Nd}/^{144}\text{Nd}$  normalization.



**Extended Data Fig. 2 | Nd isotope compositions of chondrite groups and CAIs.** The top panel shows the weighted average  $\mu^{147}\text{Nd}$  compositions for enstatite chondrites (EC), ordinary chondrites (OC), carbonaceous chondrites (CC) and CAIs. The external reproducibility of the JNdi standard (2 s.d.) is

shown for each isotope as a grey bar.  $^{143}\text{Nd}$  is not represented as any measured deviation is mostly radiogenic. The bottom panel shows the relative contributions of p-, s- and r-process nucleosynthesis for each Nd isotope are shown below as percentages<sup>10</sup>.



**Extended Data Fig. 3 | Nd isotope variations in chondrites, CAIs and accessible Earth.** **A)**  $\mu^{142}\text{Nd}$  versus  $\mu^{145}\text{Nd}$ , **B)**  $\mu^{142}\text{Nd}$  versus  $\mu^{148}\text{Nd}$ , **C)**  $\mu^{142}\text{Nd}$  versus  $\mu^{150}\text{Nd}$ , **D)**  $\mu^{148}\text{Nd}$  versus  $\mu^{150}\text{Nd}$ , **E)**  $\epsilon^{145}\text{Nd}$  versus  $\mu^{148}\text{Nd}$ , and **F)**  $\epsilon^{145}\text{Nd}$  versus  $\mu^{150}\text{Nd}$ . The modelled s-deficit lines (black) for an Earth with present-day  $\mu^{142}\text{Nd} = 0 \pm 1.1$  are plotted. Group averages are from Supplementary Tables 1 and 4: enstatite chondrites, ordinary chondrites, carbonaceous chondrites, CAIs, Allende and CAI-free Allende are plotted in each figure. Also plotted are group averages using only data from Burkhardt et al.<sup>1</sup> for enstatite chondrites, ordinary chondrites, Allende and CAI-free Allende. In each figure, the stellar s-deficit line is shown as solid black, the SIC s-deficit line is shown as dotted black and the chondrite leachate s-deficit line is shown as dashed black. For A, B and C that plot  $\mu^{142}\text{Nd}$  on the y-axis, the modelled s-deficit lines (green) for an Earth with present-day  $\mu^{142}\text{Nd} = -7.3 \pm 1.6$  (green diamond) are plotted. The mixing lines between CAIs and CAI-free Allende that go through the Allende values are shown in solid grey. All  $\mu^{142}\text{Nd}$  values for CAIs and chondrites have been corrected for radiogenic ingrowth. All uncertainties show the 95% CI for

the weighted group average. Where no error bars are shown, the symbols for the respective compositions are larger than the errors. Note that for diagrams D–F that do not plot  $\mu^{142}\text{Nd}$  on the y-axis, all Earth  $\mu^{142}\text{Nd}$  values are 0 and only one set of s-deficit lines are needed and used. In these diagrams, all of the group averages show that the differences in chondrites and Earth at 0 are consistent with s-process abundance differences and confirms earlier studies<sup>1</sup>. The deviations in the carbonaceous chondrite group average from the s-deficit lines relative to Earth in E and F, may reflect an additional and poorly constrained Nd isotope component in the CC nebular region not found in the inner Solar System. Alternatively, it may reflect the lack of removal of a CAI component in these rocks, which cannot be done without additional study (i.e. not enough data for CAIs on these meteorites). In all 6 diagrams, the group averages using all data from the literature and this study (Supplementary Table 2) are consistent within uncertainty to group averages using only data from Burkhardt et al.<sup>1</sup>. Slopes for the s-deficit lines for each diagram is from Burkhardt et al.<sup>1</sup>. See main text for additional discussion.